Article

Journal of
Nanoscience and Nanotechnology
Vol. 17, 2571–2577, 2017
www.aspbs.com/jnn

Copyright © 2017 American Scientific Publishers
All rights reserved
Printed in the United States of America

# Porous ZnO/NiO Microspherical Structures Prepared by Thermolysis of Heterobimetallic Metal-Organic Framework as Supercapacitor Electrodes

Longmei Zhang, Junhao Zhang*, Yuanjun Liu, Li Zhang, and Aihua Yuan*

*School of Environmental and Chemical Engineering, Jiangsu University of Science and Technology, Zhenjiang, Jiangsu 212003, China*

In this work, porous ZnO/NiO microspherical structures have been devised and prepared successfully via a solid-state conversion process of heterobimetallic MOF. The results of structural characterization demonstrate that the products are porous ZnO/NiO microsphereical structures with the diameter of about 2 $\mu$m, which are constructed by many interconnected nanocrystals with the sizes between 20 and 50 nm. The BET surface area of ZnO/NiO microspheres is calculated to be 170.01 $m^2\ g^{-1}$ with a broad pore size around 7.5–25 nm. Electrochemical data illuminated that the specific capacitance of the porous ZnO/NiO micro-spheres is 172.9 F $g^{-1}$ at 0.5 A $g^{-1}$. Additionally, it shows better cycling performance that the specific capacitance is 143.7 F $g^{-1}$ for the first cycle at a current density of 1 A $g^{-1}$, and still retains 140.0 F $g^{-1}$ after 2000 cycles. Importantly, this simple calcination strategy could be easily extended to prepare other porous binary metal oxide nanomaterials with specific morphologies, high porosity and excellent electrochemical performance.

Delivered by Ingenta to: State University of New York at Buffalo
IP: 128.205.44.13 On: Tue, 04 Apr 2017 15:37:07
Copyright: American Scientific Publishers

**Keywords:** MOF, ZnO/NiO, Porous Materials, Supercapacitor.

## 1. INTRODUCTION

The impending energy crisis calls for not only urgent development of clean alternative energies but also more advanced energy storage and conversion systems. Supercapacitors, also called electrochemical capacitors or ultracapacitors, have drawn significant research attention as a new class of promising energy storage devices in recent years due to their attractive properties including high power density, long cycle life, and fast charge–discharge processes.[1–3] Thus, they have dramatically increased in many areas such as digital communication devices, mobile electronic devices, back-up power supplies, and hybrid electric vehicles.[4–6] Based on the charge-storage mechanisms and active materials used, supercapacitors are divided into two categories: electric doublelayer capacitors (EDLCs) and pseudocapacitors. In electric double layer capacitors, charge is stored by rapid adsorption/desorption of electrolyte ions on high-surface-area carbon materials, a non-Faradic process. Whereas, in pseudocapacitors, charge is stored and released in Faradic electron-transfer processes of transition metal oxides or electric conducting polymers. For pseudocapacitors, charge is stored using redox-based Faradic reactions, which can have higher capacitance values than EDLCs. Among the electrode materials for supercapacitor applications, extensive attention has been paid to investigate pseudocapacitive transition metal oxides (such as $RuO_2$, $MnO_2$, NiO, $Co_3O_4$, etc.), which can obtain a higher specific capacitance and excellent energy density because they can supply a variety of oxidation states for efficient redox reactions.[7–12] Among metal oxides, $RuO_2$ has been widely studied as supercapacitor material with superior pseudocapacitive behavior, but its relatively high cost and low porosity, and toxic nature have hindered its commercial application.[8,13] Therefore, search for other cheaper complementary metal oxide materials with superior performance and environmentally friendly is important for the development of supercapacitors.

Zinc and/or nickel oxides, being cost-effective, abundant resources, environmental benign nature, and as well as excellent thermal stabilities, are a kind of promising materials that have wide applications in supercapacitors,[14] lithium-ion batteries,[15,16] and gas sensors.[17] Recently,

*Authors to whom correspondence should be addressed.

nanocomposites have attracted extensive interest for their enhanced characteristics over the single material.[18–20] For example, Cai et al. reported a unique ZnO@$Co_3O_4$ core/shell heterostructures as supercapacitor electrode, it exhibits high capacitance of 857.7 F $g^{-1}$ at a current density of 1 A $g^{-1}$, whereas $Co_3O_4$ electrode only 637.2 F $g^{-1}$.[21] We can reasonably speculate that cobalt and zinc oxide composites may result in better electrochemical characteristics, such as good electrochemical stability and high specific capacitance than those of individual ones owing to the co-contribution of both redox reactions.

Porous structures have proven to ensure efficient contact between the electrolyte and the surface of the electroactive materials and shorten the ion transport/diffusion path. Recent years, metal-organic frameworks (MOFs) have attracted much attention as sacrificial templates for devised to fabricate porous metal oxides or carbon nanostructures through thermal decomposition under controlled atmospheres.[22–26] MOFs are a class of organic–inorganic hybrid functional materials with large specific surface area and high porosity.[27] MOFs have shown promise for many applications including gas storage,[28] catalysts,[29] magnetic properties[30] and so on. Controlled synthesis of nanostructured porous electrode materials derived from the thermolysis of MOFs is still in its infancy. Obviously, how to obtain uniformed MOF nano/micro templates and inherit the morphology during the solid-state thermolysis progress is still a great challenge.

Exploring mild strategies to synthesize mesoporous materials is very important.[31] Thermal decomposition of coordination compounds micro/nanostructures is commonly used to prepare porous metal oxide materials both in the laboratory and in industry. What's more, when calcining precursor nanostructures, a large amount of gas is released during the thermal decomposition of organic ligands, and thus resulting in a novel porous structure in the products. In this work, porous ZnO/NiO microspheres with higher surface area were firstly prepared and devised by a simple calcination of heterobimetallic MOF ([ZnNi(BTC)($NO_3$)(1.6$H_2O$)](0.4DMF)) precursor in air. This strategy is simple, tunable, inexpensive, and scalable. Such porous microsphere structure is made up of many nanocrystals and nanopores, and it has large surface area which can facilitate the electron transfer and supply sufficient effective active site. Those features make the as-fabricated ZnO/NiO microspheres possess enhanced specific capacitance and long cycling stability.

## 2. EXPERIMENTAL SECTION

### 2.1. Chemicals

Nickel nitrate hexahydrate ($Ni(NO_3)_2 \cdot 6H_2O$, 99%), zinc nitrate hexahydrate ($Zn(NO_3)_2 \cdot 6H_2O$, 99%), 1,3,5-benzentricarboxylic acid ($C_6H_3(COOH)_3$, 99%), pyrazine (99%), hexadecyl trimethyl ammonium bromide (CTAB), ethanol (99.7%), *N*,*N*-dimethylformamide (DMF) were purchased from commercial suppliers (J&K reagent Co., Ltd.). All the reagents and solvents were used without further purification.

### 2.2. Synthesis of Heterobimetallic MOF Microspheres and Porous ZnO/NiO Microspheres

In a typical solvothermal procedure, 0.8 mmol nickel nitrate hexahydrate, 0.5 mmol 1,3,5-benzentricarboxylic acid, 0.7 mmol zinc nitrate hexahydrate, 1.5 mmol pyrazine and 0.3 g CTAB were dissolved in 10 mL DMF and 20 mL ethanol. After magnetically stirred for 15 minutes, the homogeneous solution was transferred into a Teflon-lined stainless steel autoclave with 40 mL capacity, and placed in an oven at 85 °C for 40 h. Finally, the resulting light green powder were collected by centrifugation and washed with ethanol for 3 times and dried at 60 °C in a vacuum oven for 12 h. The above-synthesized precursor was put into a ceramic crucible and then heated to 450 °C with a heating rate 1 °C $min^{-1}$, and maintained at 450 °C for 30 minutes under air atmosphere. Finally, porous ZnO/NiO microspheres were obtained.

### 2.3. Characterization

The crystal structure and phase purity of the products were characterized by X-ray powder diffraction (XRD) patterns, which were recorded on a MAX-RB X-ray diffractometer (Rigaku, Japan) equipped with graphite-monochromatized Cu K$\alpha$ radiation ($\lambda = 1.54178$ Å). The Fourier transform infrared (FTIR) spectrum of KBr powder pressed pellets were recorded on a Bruker Vector 22 spectrometer. The field-emission scanning electron microscopy (FESEM) images of the products were taken by a field-emission scanning electron microscope (FESEM, JEOL JSM-7600F). Transmission electron microscope (TEM) images were taken on a JEM-2100F high-resolution transmission electron microscope at an acceleration voltage of 200 kV. Energy-dispersive X-ray (EDX) analysis was performed for the products using the energy-dispersive X-ray spectroscopy attached to the JEOL JSM-7600F. X-ray photoelectron spectroscopy (XPS) of the products was performed on a Perkin-Elmer model PHI 5600 system with a monochromatic K$\alpha$ radiation (1486.6 eV) X-ray source. The nitrogen adsorption–desorption isotherms and textural properties were determined on a Micromeritics Instrument Corporation sorption analyzer (TriStar II 3020).

### 2.4. Electrochemical Measurements

Electrochemical study on porous ZnO/NiO microstructure electrodes was carried out on an electrochemical working station (AUTOlab-PGSTAT302N, Metrohm). All electrochemical performances were tested in a conventional three-electrode system. The ZnO/NiO electrode was used as the working electrode, a standard calomel electrode (SCE) electrode was the reference electrode, and a platinum electrode was used as the counter electrode, and the electrolyte

Delivered by Ingenta to: State Univ... IP: 5.101.219.231 On: Thu... Copyright: American Scientific Publishers

used was 3 mol·L$^{-1}$ KOH solution. The working electrode was made by mixing active materials (porous ZnO/NiO microspheres), acetylene black, and PTFE (polytetrafluoroethylene) at a weight ratio of 80:15:5, coating on a piece of nickel foam of about 1 cm$^2$, and pressed it at a pressure of 5.0 MPa.

## 3. RESULTS AND DISCUSSION

The Fourier transform infrared spectrum of heterobimetallic MOF was carried out at room temperature, as shown in Figure 1(a). Four distinct characteristic absorption peaks at 1611, 1560, 1447, 1370 cm$^{-1}$ are attributed to the antisymmetric stretching vibration and symmetric stretching vibrations of the C═C of 1,3,5-benzentricarboxylic acid. The weak peak around 1109 cm$^{-1}$ resulting from C–O stretching vibration. The strong and broad peak at 3417 cm$^{-1}$ is assigned to the O–H stretching vibration suggests that the O–H of the carboxylate groups is partly deprotonated,[32] which indicate that the COO$^-$ of $H_3BTC$ coordinated to Zn or Ni in a monodentate mode. What's more, the XRD patterns of as prepared heterobimetallic MOF display typical characteristic peaks (insert Fig. 1(b)) is consistent well with the simulated pattern results based on the crystal structure with the formula of $[ZnNi(BTC)(NO_3)(1.6H_2O)](0.4DMF)$, which confirms that the formula of the MOF microsphere is $[ZnNi(BTC)(NO_3)(1.6H_2O)](0.4DMF)$.[33]

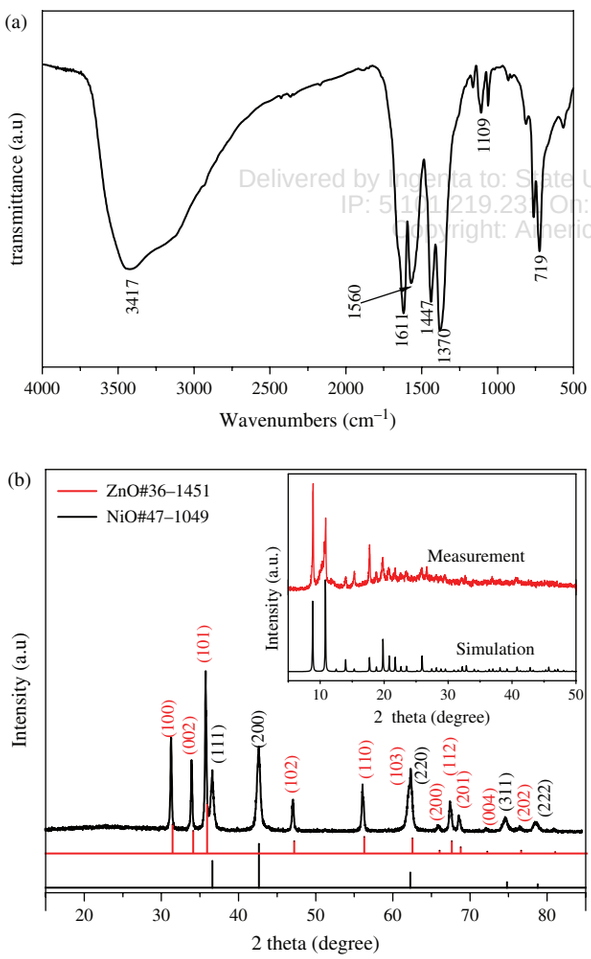


**Figure 1.** FTIR spectra of heterobimetallic MOF; (b) XRD patterns of ZnO/NiO microspheres, and insert is XRD patterns of heterobimetallic MOF.

By calcining the precursors at 450 °C for 30 minutes in air, gray powders were obtained. To investigate the crystal phases and structures of calcined products, the XRD patterns (Fig. 1(b)) were carried out. The diffraction peaks at $2\theta$ values of 31.8°, 34.4°, 36.3°, 47.5°, 56.6°, 62.9°, 66.4°, 68.0°, 69.1°, 72.6°, 76.9°, corresponding to (100), (002), (101), (102), (110), (103), (200), (112), (201), (004), and (202), respectively, can be readily indexed to hexagonal ZnO (JCPDS card no. 36-1451). The diffraction peaks at $2\theta$ values of 37.2°, 43.3°, 62.9°, 75.4°, and 79.4°, denoted as (111), (200), (220), (311), and (222), indexed to cubic NiO (JCPDS card no. 47-1049) phase crystalline structure. No other impurity peaks were detected, revealing that the micro-MOF precursors were converted to crystalline ZnO/NiO completely. Additionally, the broaden diffraction peaks indicate the small size of nanosized crystallites.

XPS have often been used to confirm the chemical composition and metal oxidation states. Here, in order to analyze the surface component of ZnO/NiO microspheres, XPS of the products were measured, which are shown in Figure 2. It can be found that the peaks on the full patterns are mainly attributed to C 1*s* (286 eV), O 1*s* (529 eV), Ni 2*p* (860 eV) and Zn 2*p* (1020 eV) and their corresponding Auger peaks in Figure 2(a), indicating the existence of carbon, oxygen, nickel and zinc element. The O 1*s* spectra at binding energies of 529.4 and 531.2 eV are ascribed to $O^{2-}$ species in ZnO/NiO microspheres.[34, 35] The binding energies of the Zn $2p_{3/2}$ and Zn $2p_{1/2}$ peaks of ZnO/NiO microspheres were found about 1021.5 and 1045 eV, indicating the existence of ZnO.[36, 37] Clearly, in the spectra of Ni 2*p* (Fig. 2(d)), the peaks centered at 851–865 eV and 870–885 eV with a main peak and satellite peak are attributed to the Ni $2p_{3/2}$ and Ni $2p_{1/2}$ spin-orbit levels of NiO.[38] The XPS results, consistent with XRD results, further prove that the as-synthesized products are ZnO/NiO composites.

The morphology of the precursor was observed by FESEM. Figure 3(a) shows that the precursors are uniform spherical structures and the average size is about 2 $\mu$m, which can be also clearly observed from the FESEM image in Figure 3(b). Typical morphologies of ZnO/NiO microspheres are presented in Figures 3(c and d). Obviously, the calcined particles retain the similar sizes and shapes as the precursor. Figure 3(c) shows that ZnO/NiO materials are still relatively uniformed spherical structures, and the distinct is that the surface of sphere-like shape becomes fairly rough compared to the precursors.

Delivered by Ingenta to: State University of New York at Binghamton
IP: 5.1.1.219.23 On: Thu, 08 Dec 2016
Copyright: American Scientific Publishers

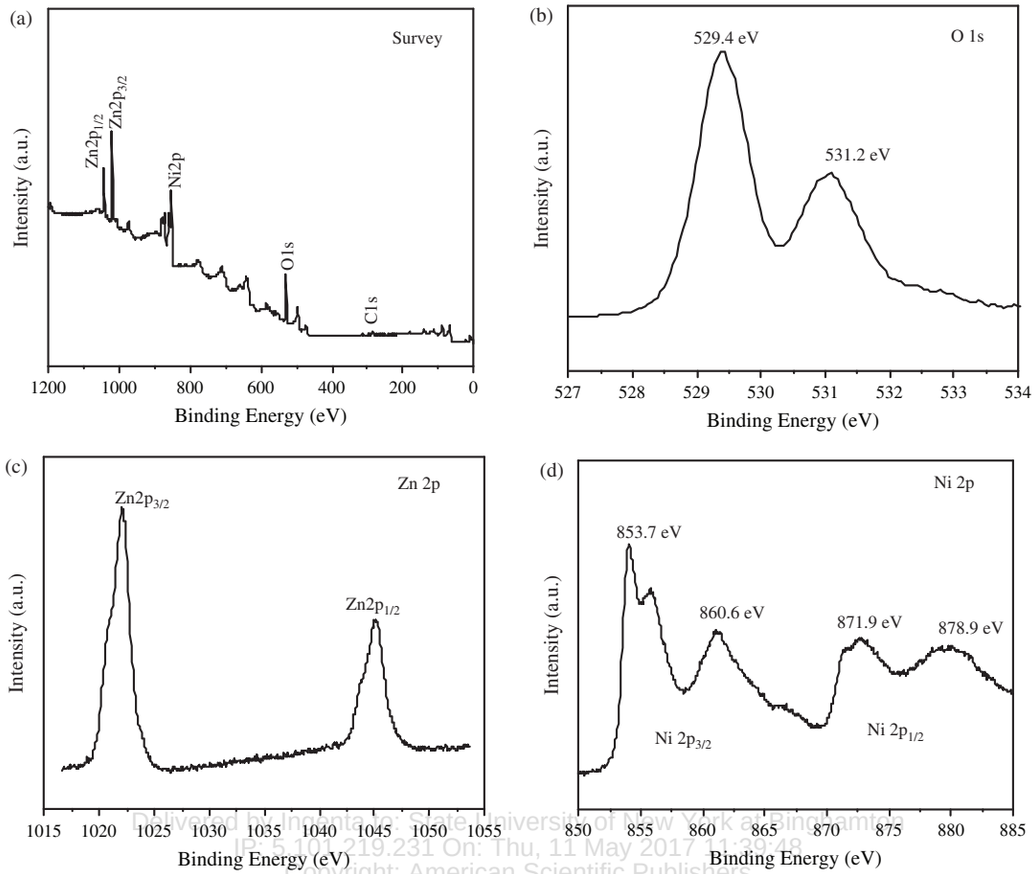


Delivered by Ingenta to: State University of New York at Binghamton
IP: 5.101.219.231 On: Thu, 11 May 2017 01:39:48
Copyright: American Scientific Publishers

**Figure 2.** XPS spectra of ZnO/NiO microspheres: (a) full survey scan spectrum; (b) O 1*s* peaks; (c) Zn 2*p* peaks; (d) Ni 2*p* peaks.

Figure 3(d) displays that ZnO/NiO materials is assembled by many uniform nanoparticles with the diameter about 50 nm. More structural informations of ZnO/NiO microspheres were investigated by TEM characterization. As shown in Figure 4(a), the projection profile of ZnO/NiO materials remains spherical-like shape, agreeing well with the morphology in the FESEM observation. Figure 4(b)

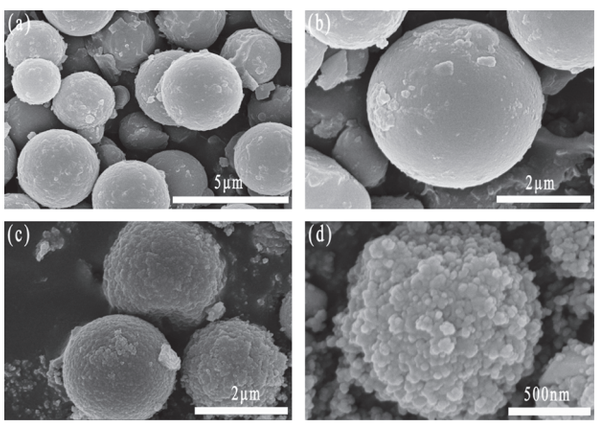


**Figure 3.** (a, b) FESEM images of precursors at different magnifications; (c, d) FESEM images of ZnO/NiO at different magnifications.

reveals that the ZnO/NiO microspheres architecture is porous structure, which is composed of numerous nanoparticles with the size ranging from 25 to 50 nm. The reason may be the successive release $CO_2$, $H_2O$ and $N_xO_y$ during the thermal decomposition of precursors. The sizes of nanoparticles are between 20 and 50 nm. The EDX spectrum in Figure 4(c) further confirm that the products contain Zn, Ni, O and C elements, and no other elements are detected, which are consistent with the results of XRD. The products include C elements, which may be from a small amount of residue of the decomposition of organic ligands.

Nitrogen absorption–desorption isotherm was carried out to obtain information about the specific surface area and pore size of the calcined samples at 77 K. In Figure 5(a), porous ZnO/NiO microspheres display typical IV adsorption–desorption isotherms with distinct hysteresis loop at a relative pressure of 0.78–1.0, which suggest the presence of mesoporous structures.[39] The pore size distribution derived from the adsorption branch using the BJH method shows that the pore size distribution is broad and around 7.5–25 nm in Figure 5(b). The Brunauer-Emmett-Teller (BET) specific surface area of porous ZnO/NiO microspheres is calculated to be 170.01 $m^2 \cdot g^{-1}$. According to the morphology and

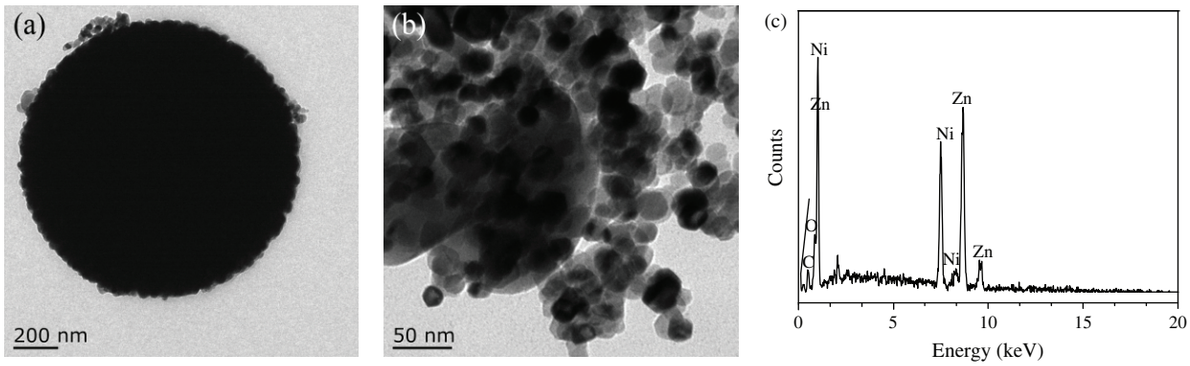


**Figure 4.** (a, b) TEM image of ZnO/NiO at different magnifications; (c) EDX spectrum of ZnO/NiO.

structural characteristics, the higher BET surface area can be attributed to porous structures and small nanoparticles.

### 3.1. Electrochemical Performances

The electrochemical properties of the porous ZnO/NiO microsphere electrode materials were investigated using a three-electrode mode by cyclic voltammetry (CV) and galvanostatic charge–discharge testing in 3 mol · $L^{-1}$ KOH electrolyte. Figure 6(a) shows the representative CV curves of the porous ZnO/NiO electrode with increasing scan rates from 5, 10, 20, to 40 mV $s^{-1}$. A distinct

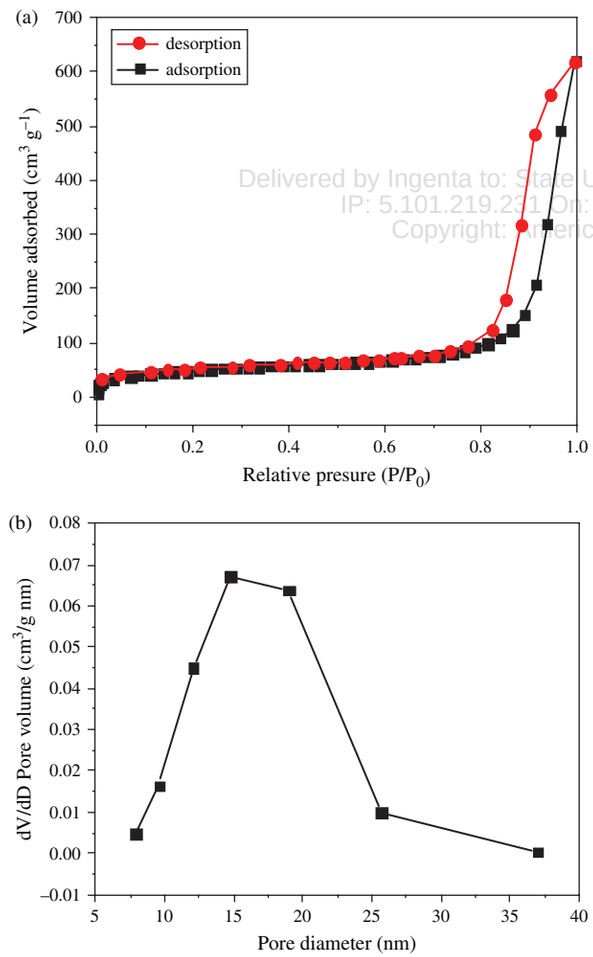


**Figure 5.** (a) $N_2$ adsorption desorption isotherms of porous ZnO/NiO microspheres; (b) Pore size distribution of porous ZnO/NiO microspheres.

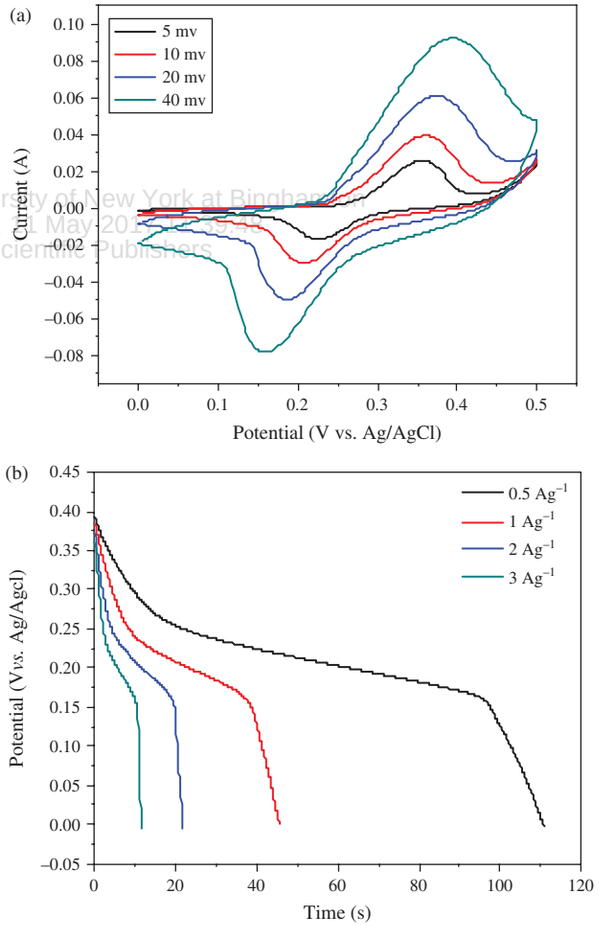


**Figure 6.** (a) Cyclic voltammograms of the porous ZnO/NiO electrode in 3 mol · $L^{-1}$ KOH electrolyte at scan rates of 5, 10, 20, 40 mV $s^{-1}$; (b) galvanostatic charge–discharge curves of the porous ZnO/NiO electrode material at charge–discharge current densities of 0.5, 1, 2 and 3 A $g^{-1}$.

Delivered by Ingenta to: State University of New York at Binghamton
IP: 5.101.219.201 On: Thu, 11 May 2017 ...
Copyright: American Scientific Publishers

pair of well-defined redox peaks is observed within the potential range 0.1–0.5 V (vs. SCE), which clearly indicates that the electrochemical capacity mainly results from pseudocapacitance behavior by two faradic redox reactions. With the scan rate increase from 5 to 40 mV $s^{-1}$, the peak current increases,[40] which suggests there is a good reversibility during the fast charge–discharge process. To further evaluate the potential application of the as-prepared ZnO/NiO sample as electrodes for ECs, galvanostatic charge–discharge measurements were carried out in 3 mol·$L^{-1}$ KOH electrolyte between 0.0 and 0.4 V (vs. Ag/AgCl) at various current densities ranging from 0.5 to 3 A $g^{-1}$, as shown in Figure 6(b). The nonlinear charge–discharge profiles further verify the pseudocapacitance behavior. The specific capacitance of the porous ZnO/NiO microsphere electrode can be calculated from charge–discharge curves by using $C = It/\Delta Vm$, where, $C$ (F $g^{-1}$) is the specific capacitance, $I$ (A) is the discharge current, $t$ (s) is the total discharge time, $\Delta V$ (V) represents the potential drop during discharge, and $m$ (g) represents the mass of ZnO/NiO within the composite electrodes. The specific capacitance values of the ZnO/NiO microsphere electrode are measured to be 172.9, 143.7, 137.5 and 107.8 F $g^{-1}$ at charge–discharge current densities of 0.5, 1, 2, and 3 A $g^{-1}$, respectively. As discharge current density increase, the specific capacitances of porous ZnO/NiO microspheres are reduced, which is the results of the resistance increase in porous ZnO/NiO microspheres and the relatively insufficient faradic redox reaction at higher current densities.

The long-term cycling stability of the porous ZnO/NiO electrode is also an important requirement for practical supercapacitor applications, which was investigated by repeated charge–discharge measurement at constant current density of 1 A $g^{-1}$ for 2000 cycles. Figure 7 shows the specific capacitance variation of the ZnO/NiO samples as a function of cycle number within a voltage range from 0.0 and 0.4 V in 3 mol·$L^{-1}$ KOH electrolyte. It was seen that the specific capacitance of the ZnO/NiO electrode is 143.7 F $g^{-1}$ in the first cycle, and it gradually decreases to 140.0 F $g^{-1}$ after 2000 cycles, which only reduces 2.5%. There is no significant capacitance loss observed over 2000 cycles at a high current density of 1 A $g^{-1}$, which is attributed to that the specific porous space of the ZnO/NiO electrode can serve as a robust reservoir for ions, and enhance the diffusion kinetics. Moreover, the porous channels ensure efficient contact between the electrolyte and the surface of the electroactive particles, which was verified in previously reported results.[41] Additionally, the porous structures of the ZnO/NiO materials lead to higher specific surface area, which can provide many surface electroactive sites for redox pseudocapacitance and further improves the surface adsorption–desorption process of alkali cations. The advantageous high porosity can also shorten the ion transport/diffusion path that leads to fast kinetics for both electrons and ions within the oxides, resulting in reduced internal resistance and improved high-power performance. The insert in Figure 7 shows the initial and last 5 galvanostatic charge–discharge cycles of the ZnO/NiO electrode in 3 mol·$L^{-1}$ KOH solution at 1 A $g^{-1}$, respectively. The results display that the charge–discharge process is highly reversible. The charge–discharge curve is asymmetric in the first 5 cycles, and also the shapes of the two curves remain the same during the charge–discharge process. The cycling life test suggests that the porous ZnO/NiO nano/micro superstructures electrode has high stability for long-term applications.

Delivered by Ingenta to: University of Waterloo
IP: 129.97.124.241 On: Thu, 11 May 2017 12:58:42
Copyright: American Scientific Publishers

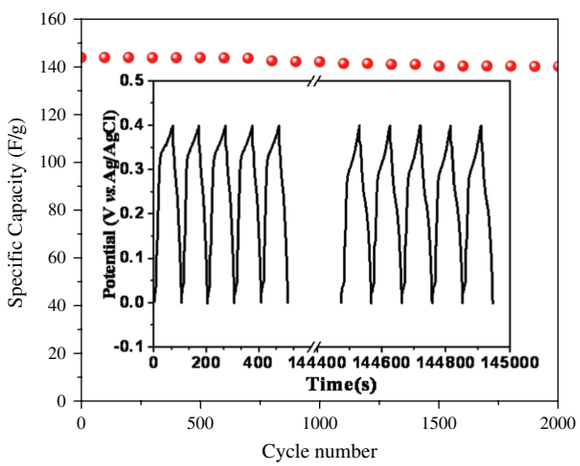


**Figure 7.** Cycling performance of the porous ZnO/NiO electrode at a current density of 1 A $g^{-1}$ and in the insert is the first and last 5 cycles of the porous ZnO/NiO electrode material at 1 A $g^{-1}$.

## 4. CONCLUSION

In summary, porous ZnO/NiO microspheres were prepared by solid-state thermal decomposition from micro-heterobimetallic MOF crystal and were consequently applied as an electrode material for supercapacitors. Electrochemical results indicate that the as prepared porous ZnO/NiO electrode could deliver a specific capacitance of 172.9 F $g^{-1}$ at a current density of 0.5 A $g^{-1}$. Additionally, it also displays excellent recycling stability that the specific capacitance is 143.7 F $g^{-1}$ for the first cycle at a current density of 1 A $g^{-1}$, and still retains 140.0 F $g^{-1}$ after 2000 cycles, which only reduces 2.5%. It is expected that the facile solid-phase conversion approach can be viable extended to prepare other porous metal oxide-based functional materials with well-defined morphologies. This class of function materials might have great potential applications in energy devices such as supercapacitors and lithium ion batteries.

**Acknowledgment:** The work was financially supported by National Natural Science Foundation of China

(51072072, 51272095), Natural Science Foundation of Jiangsu Province (No. BK20141293), Natural Science Foundation of the Higher Education Institutions of Jiangsu Province (No. 13KJB430012), the Opening Project of State Key Laboratory of Fire Science (No. HZ2015-KF03), and Qing Lan Project of Jiangsu Province (No. 1614101401). The authors declare no competing financial interest.

## References and Notes

1. S. Ratha and C. S. Rout, *RSC Adv.* 5, 86551 (**2015**).
2. Q. F. Zhang, E. Uchaker, S. L. Candelari, and G. Z. Cao, *Chem. Soc. Rev.* 42, 3127 (**2013**).
3. X. Zhao, B. M. Sánchez, P. J. Dobsona, and P. S. Grant, *Nanoscale* 3, 839 (**2011**).
4. V. Subramanian, H. W. Zhu, R. Vajtai, P. M. Ajayan, and B. Q. Wei, *J. Phys. Chem. B* 109, 20207 (**2005**).
5. A. S. Aricò, P. Bruce, B. Scrosati, J. M. Tarascon, and W. van Schalkwijk, *Nat. Mater.* 4, 366 (**2005**).
6. S. Faraji and F. N. Ani, *Renewable and Sustainable Energy Reviews* 42, 823 (**2015**).
7. X. Wu, Y. Zeng, H. R. Gao, J. Su, J. P. Liu, and Z. H. Zhu, *J. Mater. Chem. A* 1, 469 (**2013**).
8. R. Silva, G. M. Pereira, D. Voiry, M. Chhowalla, and T. Asefa, *RSC Adv.* 5, 49385 (**2015**).
9. W. F. Wei, X. W. Cui, W. X. Chen, and D. G. Ivey, *Chem. Soc. Rev.* 40, 1697 (**2011**).
10. T. Zhu, J. S. Chen, and X. W. Lou, *J. Mater. Chem.* 20, 7015 (**2010**).
11. Q. Yang, Z. Y. Lu, Z. Chang, W. Zhu, J. Q. Sun, J. F. Liu, X. M. Sun, and X. Duan, *RSC Adv.* 2, 1663 (**2012**).
12. J. H. Zhang, S. Wan, B. Yan, L. B. Wang, and Y. T. Qian, *J. Nanosci. Nanotechn.* 13, 4364 (**2013**).
13. R. B. Rakhi, W. Chen, D. Cha, and H. N. Alshareef, *J. Mater. Chem.* 21, 16197 (**2011**).
14. X. Zhang, Y. Q. Zhao, C. L. Xu, X. Zhang, Y. Zhao, and C. Xu, *Nanoscale* 6, 3638 (**2014**).
15. C. Li, T. Q. Chen, W. J. Xu, X. B. Lou, L. K. Pan, Q. Chen, and B. W. Hu, *J. Mater. Chem. A* 3, 5585 (**2015**).
16. S. J. Yang, S. Nam, T. Kim, J. H. Im, H. Jung, J. H. Kang, S. Wi, B. Park, and C. R. Park, *J. Am. Chem. Soc.* 135, 7394 (**2013**).
17. Y. J. Liu, G. X. Zhu, J. Z. Chen, H. Xu, X. P. Shen, and A. H. Yuan, *Appl. Surf. Sci.* 265, 379 (**2013**).
18. C. C. Hua, H. Y. Guo, K. H. Chang, and C. C. Huang, *Electrochem. Commun.* 11, 1631 (**2009**).
19. T. E. Quickel, V. H. Le, T. Brezesinski, and S. H. Tolbert, *Nano Lett.* 10, 2982 (**2010**).
20. J. H. Zhang, K. Yanagisawa, S. S. Yao, H. T. Wong, Y. S. Qiu, and H. J. Zheng, *J. Mater. Chem. A* 3, 7877 (**2015**).
21. D. P. Cai, H. Huang, D. D. Wang, B. Liu, L. L. Wang, Y. Liu, Q. H. Li, and T. L. Wang, *ACS Appl. Mater. Interfaces* 6, 15905 (**2014**).
22. H. L. Jiang and Q. Xu, *Chem. Commun.* 47, 3351 (**2011**).
23. B. Yan, L. Chen, Y. J. Liu, G. X. Zhu, C. G. Wang, H. Zhang, G. Yang, H. T. Ye, and A. H. Yuan, *CrystEngComm.* 16, 10227 (**2014**).
24. M. Hu, A. A. Belik, M. Imura, K. Mibu, Y. Tsujimoto, and Y. Yamauchi, *Chem. Mater.* 24, 2698 (**2012**).
25. R. B. Wu, X. K. Qian, F. Yu, H. Liu, K. Zhou, J. Wei, and Y. Z. Huang, *J. Mater. Chem. A* 1, 11126 (**2013**).
26. R. B. Wu, X. K. Qian, Xi. H. Rui, H. Liu, B. Yadian, K. Zhou, J. Wei, Q. Y. Yan X. Q. Feng, Y. Long, L. Y. Wang, and Y. Z. Huang, *Small* 10, 1932 (**2014**).
27. H. Furukawa, U. Müller, and O. M. Yaghi, *Angew. Chem. Int. Ed.* 54, 3417 (**2015**).
28. H. Zhou, X. Q. Liu, J. Zhang, X. F. Yan, Y. J. Liu, and A. H. Yuan, *Int. J. Hydrogen Energ.* 39, 2160 (**2014**).
29. J. S. Seo, D. Whang, H. Lee, S. I. Jun, J. Oh, Y. J. Jeon, and K. Kim, *Nature* 404, 982 (**2000**).
30. D. Y. Yu, L. Li, H. Zhou, A. H. Yuan, and L. Z. Li, *Eur. J. Inorg. Chem.* 2012, 3394 (**2012**).
31. V. Malgras, Q. Ji, Y. Kamachi, T. Mori, F. K. Shieh, K. C. W. Wu, K. Ariga, and Y. Yamauchi, *Bull. Chem. Soc. Jpn.* 88, 1171 (**2015**).
32. F. L. Meng, Z. G. Fang, Z. X. Li, W. W. Xu, M. J. Wang, Y. P. Liu, J. Zhang, W. R. Wang, D. Y. Zhao, and X. H. Guo, *J. Mater. Chem. A* 1, 7235 (**2013**).
33. J. S. Chen, T. Zhu, Q. H. Hu, J. J. Gao, F. B. Su, S. Z. Qiao, and X. W. Lou, *ACS Appl. Mater. Interfaces* 2, 3628 (**2010**).
34. Y. E. Roginskaya, O. V. Morozova, E. N. Lubnin, Y. E. Ulitina, G. V. Lopukhova, and S. Trasatti, *Langmuir* 13, 4621 (**1997**).
35. J. H. Zhang, J. Du, Y. T. Qian, Q. H. Yin, and D. J. Zhang, *Metal. Sci. Eng. B* 170, 51 (**2010**).
36. T. F. Hung, S. G. Mohamed, C. C. Shen, Y. Q. Tsai, W. S. Chang, and R. S. Liu, *Nanoscale* 5, 12115 (**2013**).
37. H. Y. Yue, Z. P. Shi, Q. X. Wang, Z. X. Cao, H. Y. Dong, Y. Qiao, Y. H. Yin, and S. Yang, *ACS Appl. Mater. Interfaces* 6, 17067 (**2014**).
38. G. M. Zhou, D. W. Wang, L. C. Yin, N. Li, F. Li, and H. M. Cheng, *ACS Nano* 6, 3214 (**2012**).
39. J. H. Zhang, J. Du, Y. T. Qian, and S. L. Xiong, *Mater. Res. Bull.* 45, 15 (**2010**).
40. L. B. Kong, J. W. Lang, M. Liu, Y. C. Luo, and L. Kang, *J. Power Sources* 194, 1194 (**2009**).
41. C. Z. Yuan, J. Y. Li, L. R. Hou, X. G. Zhang, L. F. Shen, and X. W. Lou, *Advanced Funct. Mater.* 22, 4592 (**2012**).

Delivered by Ingenta to: State University of New York at Binghamton
IP: 128.101.219.231 On: Thu, 11 May 2017 21:29:48
Copyright: American Scientific Publishers

Received: 13 November 2015. Accepted: 12 December 2015.